Dissolution and Bandgap paradigms for predicting the toxicity of metal oxide nanoparticles in the marine environment: an *in vivo* study with oyster embryos

Seta Noventa*, Christian Hacker, Darren Rowe, Christine Elgy and Tamara Galloway

Seta Noventa = College of Life and Environmental Sciences, University of Exeter, EX4 4QD, Exeter UK, tel 01392 263436 email s.noventa2@exeter.ac.uk, *corresponding author

Christian Hacker = College of Life and Environmental Sciences, Bioimaging Centre, University of Exeter, EX4 4QD, Exeter UK; C.Hacker@exeter.ac.uk

Darren Rowe = College of Life and Environmental Sciences, University of Exeter, EX4 4QD, Exeter UK; Darren.Rowe@exeter.ac.uk

Christine Elgy = Department of Geography, Earth and Environmental Sciences, Facility for Environmental Nanoscience Analysis and Characterisation, University of Birmingham, Edgbaston, Birmingham, UK; C.N.Elgy@bham.ac.uk

Tamara Galloway = College of Life and Environmental Sciences, University of Exeter, EX4 4QD, Exeter UK; T.S.Galloway@exeter.ac.uk

Abstract

Dissolution and bandgap paradigms have been proposed for predicting the ability of metal oxide nanoparticles (NPs) to induce oxidative stress in different *in vitro and in vivo* models. Here we addressed the effectiveness of these paradigms *in vivo* and under conditions typical of the marine environment, a final sink for many NPs released through aquatic systems. We used ZnO and MnO_2 NPs as models for dissolution and bandgap paradigms, respectively, and CeO_2 NPs to assess reactive oxygen radical (ROS) production via Fenton-like reactions *in vivo*. Oyster embryos were exposed to 0.5-500 µM of each test NP over 24 h and oxidative stress was determined as a primary toxicity pathway across successive levels of biological complexity, with arrested development as the main pathological outcome. NPs were actively ingested by oyster larvae and entered cells. Dissolution was a viable paradigm for predicting the toxicity of NPs in the marine environment, whereas the surface reactivity based paradigms (i.e. bandgap and ROS generation via Fenton-like reaction) were not supported under seawater conditions. Bio-imaging identified potential cellular storage-disposal sites of solid particles that could ameliorate the toxicological behavior of non-dissolving NPs, whilst abiotic screening of surface reactivity suggested that the adsorption-complexation of surface active sites by seawater ions could provide a valuable hypothesis to explain the quenching of the intrinsic oxidation potential of MnO_2 NPs in seawater.

Keywords

Metal oxide nanoparticles; oxidative stress; *in vivo* toxicity; seawater; oyster*.*

1   Introduction

Metal oxide nanoparticles (MOx NPs) are a commercially important class of engineered nanomaterials. Thanks to their semiconducting properties, they are produced in large volume for a wide spectrum of nanotechnology applications, increasing the risk of exposure to humans and natural environments (Joo and Zhao, 2017). Laboratory experiments have shown that MOx NPs can come into contact with molecular-cellular structures and interfere with processes occurring at the nanoscale. In biological environments, MOx NPs can act as electronically active substrates for reactions with cellular redox pairs and oxygen species, with the potential for direct or reactive oxygen species (ROS) mediated cytotoxicity (He *et al.*, 2015). The development of appropriate safety assessment, including a reliable and reproducible screening approach for ranking MOx NP hazard, remains a challenge since the type of interaction at the nano/bio interface largely depends on distinctive 'product-specific' proprieties, such as composition, size, surface area, shape, dispensability, aggregation, crystallinity, surface functionalization and coating. Structure-activity based paradigms provide a valuable aid for predicting potential human and environmental hazards for such a wide variety of substances. To be effective, the invoked paradigms need to relate 1) NP physical-chemical properties with toxicity pathways, and 2) induced cellular responses with pathogenesis *in vivo* (Liu *et al.*, 2013, Tantra *et al.*, 2015). The induction of oxidative stress is a plausible mechanistic pathway for this purpose. Significant disruption of cellular redox homeostasis correlates well with pro-inflammatory effects in cellular models and disease outcomes *in vivo* (Xia *et al.*, 2008, Zhang *et al.*, 2012, Kaweeteerawat *et al.*, 2015). This concept has previously been framed into the *hierarchical oxidative stress* paradigm, which classifies imbalance of the redox cellular steady state based on the progressive induction of 1) cellular antioxidant defence, 2) pro-inflammatory responses and 3) cytotoxicity (Nel *et al.*, 2006, Meng *et al.*, 2009).

When screening the oxidation potential of twenty-four MOx NPs for structure–activity relationships, the most toxic NPs were those that featured either a high rate of metal dissolution (i.e. ZnO and CuO NPs) or conduction band energy values between -4.12 and -4.84 eV (i.e. Ni_2O_3, CoO, Cr_2O_3, Co_3O_4, and Mn_2O_3 NPs) (Zhang *et al.*, 2012, Kaweeteerawat *et al.*, 2015). The first mode of action based on dissolution refers to the potential for release from NPs of cytotoxic concentrations of metal ions into the media and directly inside cells (i.e. *Trojan horse mechanism*). The second mechanism (i.e. *bandgap*) concerns direct electron transfer between MOx NPs and cellular targets, which is enabled when the energy of their

2

exchangeable electrons align, enabling the oxidation of cellular components, the generation of ROS and inducing toxicity (Burello and Worth, 2011a).

While the effectiveness of the dissolution-bandgap and *hierarchical oxidative stress* paradigms has been extensively demonstrated using both *in vitro* and *in vivo* models (Zhang *et al.*, 2012, Kaweeteerawat *et al.*, 2015, Delaval *et al.*, 2017), their suitability for predicting MOx NPs toxicity under realistic environmental scenarios has not been addressed. The marine environment is one of the final sinks for engineered nanomaterials released through water systems and, once there, nanomaterials undergo drastic physico-chemical change which alters their reactivity, behavior and fate. In particular, the high concentration of ions and the presence of natural organic matter in seawater can modify MOx NP surface stability and reactivity, and drive their biological fate (Klaine *et al.*, 2008).

Here, we explored the validity of dissolution and bandgap paradigms for predicting toxicity *in vivo* and under conditions typical of the marine environment. We selected ZnO and MnO_2 NPs as models for dissolution and bandgap paradigms, respectively, based on their published mode of action (Burello and Worth, 2011b, Zhang *et al.*, 2012).CeO_2 NPs were included to assess the contribution of reactive oxygen species (ROS) production via reaction with H_2O_2 (i.e. Fenton-like reaction). Due to the Ce oxidation states available on CeO_2 NPs surface (i.e. Ce^{3+}/Ce^{4+}), this nanomaterial exhibits pro-oxidant or superoxide (SOD)-mimicking behavior under different experimental conditions (Collin *et al.*, 2014, Nelson *et al.*, 2016). The hypotheses were tested using oyster embryo-larvae (*Crassostrea gigas*) as the model organism, *hierarchical oxidative stress* as a primary toxic pathway, and arrested development of embryos into D-shaped shell larvae as the main pathological outcome. Oyster embryos were exposed to increasing concentrations of each test NP over 24 h; to assess the induction of the oxidative stress machinery, we used a multi-parameter screening system (Zhang *et al.*, 2012) across increasing levels of toxicity (i.e. from cellular antioxidant defence to cytotoxicity) and over different orders of biological organization (i.e. from genomics to whole organism).

The oyster *C. gigas* is a well-characterized marine invertebrate of high economic and ecological importance (Guo *et al.*, 2015). In extrapolating the *hierarchical oxidative stress* pathway to the *C. gigas* embryo-larval model, we considered the specificity of the molecular mechanisms in oyster species and their ontogenesis (Montagnani *et al.*, 2004, Tirapé *et al.*, 2007, Zhang *et al.*, 2011, Sussarellu *et al.*, 2012, Genard *et al.*, 2013, Li *et al.*, 2013, Zhang *et al.*, 2013, Mai *et al.*, 2014, Song *et al.*, 2016). The predictive ability of the test paradigms was addressed by considering seawater cation-driven changes in the physical-chemical proprieties of MOx NPs. We investigated the bioavailability of the test NPs and retention of their oxidation potential once dispersed in artificial seawater (ASW) since aggregation of NPs in ionic solutions can alter filtration and ingestion by feeding larvae (i.e. trochophore and D-

shaped veliger), and consequent internalization. Furthermore, the influence of ASW on both dissolution and NP surface reactivity was considered since these processes can be significantly challenged by seawater ions via the adsorption-complexation of their reactive sites, redox shift and decrease of the surface-to-volume ratio.

2 Materials and methods

2.1 Nanoparticles

2.1.1 **NP supply and primary features**

The primary physico-chemical properties of the three test NPs are summarized in table S1 of the Supporting Information (SI). CeO_2 NPs (NM-211) were obtained from the European Nanomaterial Repository (Joint Research Center, Ispra, Italy), and ZnO NPs (NM-110) from the OECD sponsorship programme for the global safety assessment of nanomaterials (www.nanotechia-prospect.org). The main primary physico-chemical proprieties of these two test NPs were retrieved from the official reports (JRC64075, 2011, JRC89825, 2014) and from the literature (Dogra *et al.*, 2016). The pH at the isoelectric point (pH_{IEP}) for each NP was determined through the electrokinetic method at the NERC Facility for Environmental Nanoscience Analysis and Characterisation (FENAC, Birmingham, UK).

Manganese oxide NPs (4910DX) were purchased from Skyspring Nanomaterials Inc (Houston, USA) and were characterized at FENAC in terms of primary structure (i.e. primary shape and size; Transmission Electron Microscopy, TEM), crystal structure (X-ray powder diffraction, XRD), surface area (Branauer, Emmett and Teller, BET) and pH_{IEP} (electrokinetic method). All the methods are detailed in the SI. Contrary to the claim of the manufacturer (i.e. Mn_2O_3 nanopowder), the X-ray diffraction (XRD) characterization identified the manganese oxide nanomaterial as $Mn^{4+}O_2$ (i.e. Akhtenskite synthetic ICDD card 01-089-5171). The experimental XRD pattern was distinct from both pure Mn^{3+} oxide minerals (i.e. Bixbyite-C syn, Mn_2O_3, ICDD card 00-041-1442) and Mn^{3+}/Mn^{4+} oxide minerals (i.e. Hausmannite, Mn_3O_4, ICDD card 00-024-0734, 01-080-0382) (shown in the SI). As detailed in section 3.3.2, the suitability of this nanomaterial as a model for the bandgap paradigm (Zhang *et al.*, 2012) was assessed from the overlap of its bandgap with the energy range of interest (-4.12 and -4.84 eV) (i.e. cytochrome c oxidation assay, method described in section 2.4.2).

2.2 In vivo oyster embryo exposures

2.2.1 **NP seawater suspensions**

For *in vivo* exposure for 24 h of oyster embryos, NP suspensions were prepared freshly before use by diluting the NP stock suspension in ASW (Tropic Marin®SEA SALT, salinity 30.0±0.2 ppt; final volume 1L). The NP stock suspensions were made up by following the standard operation protocol developed under the PROPECT project (Ecotoxicology Test Protocols for

Representative Nanomaterials in Support of the OECD Sponsorship Programme; PROSPECT, 2010; http://www.nanotechia.org). Briefly, 25.0 mg NP powders were weighed in 30 mL glass vials and made into a paste by adding a few drops of deionized water (DIW). Then 25 mL of DIW were added to the paste and the suspension was sonicated for 30 secs (ultrasonic probe, 90% amplitude; Cole Parmer 130 W Ultrasonic Processor). At the start of the experiment, stock solution was added into each exposure chamber, as detailed below.

2.2.2 Oyster fertilization and *in vivo* exposure of embryos

Conditioned oysters were purchased from the Guernsey Sea Farm Ltd. hatchery (Guernsey, UK). The ICES protocol n°54 (Leverett D, 2013) was followed for fertilization. Briefly, embryos were obtained from three pairs of parental adults. Male and female gametes were obtained by gently cutting the gonads with a sharp scalpel, and the recovered egg suspension was fertilized by adding a few milliliters of sperm. Once the polar body was visible on 80-90% of the eggs, the fertilized eggs were incubated for 2 h at 24°C, in dark conditions and without aeration. At the achievement of the 16-32 cell stage, embryos were transferred at a density of 250 embryos mL^{-1} into the exposure chambers, previously filled with 1 L of ASW properly dosed with the NP stock solutions. For all test NPs, the exposure concentrations were 0.5, 5, 50, 500 µM (plus negative control). The *in vivo* exposures were carried out for 24 h under static conditions (ASW at 30 ± 0.2 ppt salinity, pH =8.10 ± 0.05; 12:12h light/dark cycle, no aeration). Three independent biological replicates were set for each exposure condition.

At the end of the exposure, embryos were filtered through a 25 µm mesh sieve and aliquots stored for biological analyses (samples for genomics and functional analyses were snap frozen in liquid N_2 and stored at −80°C; samples for embryotoxicity assay were fixed via buffered formaldehyde solution; samples for TEM imaging were fixed in 3%glutaraldehyde/2% paraformaldehyde in 0.1 M Pipes buffer, pH 7.2, for 2 h at room temperature, and then kept at +4°C until embedding). In accordance with the ICES protocol, the performance of the exposure was established by assessing the normal development of the D-shaped shell in at least the 70% of larvae in the control (at 26 hours post-fertilization, hpf).

2.2.3 TEM-EDS analysis of NP biological fate

The biological fate of the test NPs in the model organism (i.e. NPs ingestion, internalization) was evaluated by optical microscopy (Zeiss Axio Observer Inverted Microscope) and transmission electron microscopy coupled with energy dispersive X-ray spectroscopy (TEM-EDS; JEOL JEM-2100 LaB6 200 kV TEM with Oxford INCA EDS). For TEM-EDS imaging, fixed larvae (3%glutaraldehyde/2% paraformaldehyde in 0.1 M Pipes buffer, pH 7.2) were washed 3 x 5 mins in buffer before post-fixation in 1% osmium tetroxide (reduced with 1.5% potassium hexacyanoferrate in DIW) in 0.1M sodium cacodylate (pH 7.2) for 1 h. After 3 washes in DIW the samples were dehydrated through a graded ethanol series followed by

embedment in Spurr resin (TAAB, Aldermaston, UK). Ultrathin sections of 80 nm were collected on pioloform-coated 100 mesh copper TEM grids (Agar Scientific, Stansted, UK) and examined using a JEOL JEM 1400 TEM operated at 120 kV (digital camera ES 100W CCD, Gatan, Abingdon, UK).

2.3 Oxidative stress screening

The induction of oxidative stress caused by the ingested NPs in the exposed larvae was evaluated according to the *hierarchical oxidative stress paradigm* (*tier 1*: cellular antioxidant defence; *tier 2*: pro-inflammatory responses; *tier 3*: cytotoxicity) accounting for different levels of biological complexity (i.e. gene expression, cellular functioning and organism health status). Genomics analysis examined the expression of five genes (*tier 1:* metallothionein 2, MT2; mitochondrial superoxide dismutase, SODmt; catalase, CAT; *tier 2:* allograft inflammatory factor-1, AIF-1; *tier 3:* inhibitors of apoptosis proteins, IAPs). At the cellular level, SOD activity (*tier 1*) and lipid peroxidation (*tier 3*) were measured. Finally, as a marker of pathogenesis at the organism level, the arrested development of embryos into the D-shaped larval stage was assessed.

2.3.1 **Gene expression**

Relative expression of the selected genes was determined through reverse-transcription and quantitative polymerase chain reaction (RT-qPCR) analysis. Embryo samples were homogenized with a pestle and total RNA extracted using Trizol, followed by DNase treatment (RQ1 RNase-Free DNase, Promega, Southampton, UK; manufacturer's protocol). cDNA was synthesized from 2 µg RNA using oligo dT and M-MLV Reverse Transcriptasis (Promega, Southampton, UK; manufacturer's protocol). The expression of target genes was determined using primer sequences (Table S3 in the SI). qPCR was performed by using iTaq Universal SYBR Green Supermix (Bio-Rad) and iCycler iQ Real-time detection system (Bio-Rad Laboratories Inc., CA, USA). More details about qPCR conditions and amplification performance are reported in Table S3 (SI).

The relative expression of each gene transcript was calculated as described by Vogeler and collaborators (Vogeler *et al.*, 2016). Briefly, the mean C_t value of each biological replicate was corrected for amplification efficiency and compared to the normalization factor obtained from the expression of three housekeeping genes (i.e. elongation factor-1, EF-1; ribosomal protein S18, RS18; actin). For each target gene, the expression ratios between treated samples and control were computed by using the comparative C_t method (i.e. $2^{-\Delta\Delta Ct}$).

2.3.2 **Cell function**

Oyster embryo samples were homogenized under ice-cold conditions before spectrophotometric analyses of SOD activity and lipid peroxidation. Both colorimetric

methods, based on the use of a 96-well plate reader (Tecan Infinite® 200 PRO series plate reader). Briefly, the activity of SOD (i.e. reduction of superoxide ions levels generated by xanthine–xanthine oxidase) was determined in terms of inhibition of the formazan dye formation (i.e. the product of tetrazolium salt reduction by superoxide ions) as described (Dogra *et al.*, 2016). Total lipid peroxidation products were measured by the thiobarbituric acid reacting substances (TBARS) assay (Camejo *et al.*, 1998, Dogra *et al.*, 2016). All data from the assays were normalized per mg of cell protein. Total protein concentration was assayed by the BioRad protein micro-assay method, using BSA as standard (manufacturer's protocol).

2.3.3 **Embryotoxicity**

The assessment of embryotoxicity followed ICES protocol n°54 (Leverett D, 2013). Fixed embryo samples were scored using inverted microscopy (Zeiss Axio Observer Inverted Microscope) to assess the percentage of embryos developing normally into D-shaped larvae (26 hpf). Normally developed D-larvae exhibited a fully developed and symmetrical shell. A total of 100 individual organisms were scored for each sample.

2.4 **Characterization of the behaviour of the test NPs**

2.4.1 **Dissolution**

Dissolution was assessed in DIW media for all test NPs and in ASW to evaluate the influence of seawater on the dissolution model NPs (i.e. ZnO NPs). In brief, the extent of NP dissolution was assessed after 24 h weathering in DIW and ASW (24°C) via ultrafiltration (3 KDa Microsep™ Advance Centrifugal Devices, Pall Life Sciences), followed by microwave assisted acid digestion (2 mL of sample, 1 mL of HNO_3; Ethos EZ, Milestone Inc, Shelton) and elemental analysis (Inductively coupled plasma - mass spectrometry, ICP-MS; Thermo Scientific X Series 2). The method is detailed in the SI.

2.4.2 **Surface reactivity**

Two abiotic assays were carried out to assess the test NP surface oxidation potential according to the modes of action of interest (i.e. bandgap mechanism; ROS generation via reaction with H_2O_2) and the potential influence of seawater ions.

In brief, the efficiency of the bandgap mechanism was tested through the acellular cytochrome *c* (cyt c) oxidation assay, (Zhang *et al.*, 2012), using a high throughput method (Delaval *et al.*, 2017). This abiotic assay assesses the overlap of the bandgap of test NPs (i.e. conduction band energy level) with the energy range of interest (-4.12 and -4.84 eV) by evaluating oxidation of the cyt c hemeprotein, a potential cellular redox target, via direct electron transfer. The production of ROS by all test MOx NPs via reaction with H_2O_2 was determined using the plasmid relaxation assay (Dogra *et al.*, 2016), which assesses covalent damage caused by ROS to biological material, in the form of plasmid supercoiled circular DNA (pBR322;

Promega, Southampton, UK). The occurrence of single and double strand breaks to circular supercoiled DNA was determined via gel electrophoresis to separate nicked-open circular DNA (i.e. single strand breaks), linear DNA (i.e. double strand break) and supercoiled circular DNA (i.e. undamaged DNA). All methods are detailed in the SI.

2.4.3 **Hydrodynamic size**

The hydrodynamic diameter of NPs in ASW dispersions (50 µM) was measured using a Zetasizer Nano ZS ZEN3600 (Malvern Instruments Ltd. Malvern, UK) operating with a He-Ne laser at a wavelength of 633 nm using back scattered light. Samples were held at 20ºC for 2 mins prior to analysis to allow for particle stabilisation. Ten replicate measurements were made on each sample and data are reported as means and the standard deviations of the replicates.

2.5   Statistical analysis

ANOVA one-way followed by Tukey HDS post-hoc test (n=3, p-value=0.05) was used to assess differences in target gene expression, physiological responses and embryotoxicity between controls and NP exposed samples. The statistical analysis was carried out using STATISTICA 8.0 StatSoft.

3   Results

3.1   NP ingestion and internalization

Optical microscope imaging of D-shaped shell larvae clearly showed the presence of NP clumps in the visceral mass, close to the shell hinge (Figure 1A-B). Transmission electron microscopy - energy dispersive X-ray spectroscopy (TEM-EDS) localized these NP aggregates inside the digestive tract and among the cilia of the retracted velum (Figure 1C-E; EDS spectra are reported in the SI). This indicates the compatibility in size between the NP aggregates in ASW and the larval particle filtration and sorting system, allowing for ingestion of NPs by the oyster larvae (i.e. trochophores and D-shaped shell larvae). The TEM images revealed that the NP aggregates concentrated inside the lumen of the digestive organs were up to 600 nm in size. Single particles were also visible, possibly disaggregating from the large aggregates.

The cellular uptake of ingested NPs was studied only for one of the non-dissolving nanomaterials (i.e. MnO_2 NPs), as the cellular entry of the particle forms is a crucial bottle-neck to their overall toxicological activity. We opted for MnO_2 NPs, since internalization evidence for this nanomaterial is in general less reported compared to CeO_2 NPs (Plascencia-Villa et al., 2012, Mazzolini et al., 2016, Ferraro et al., 2017). Electron dense particles, identified as MnO_2 NPs by EDS analysis, were observed inside single-membrane bound

bodies which are likely to represent endosomal structures (Figure 2A-B; EDS spectra is reported in the SI). The size of these particles (i.e. ~ 50 nm) was consistent with the primary size of MnO_2 NPs.

Interestingly, large NP aggregates (up to 200 nm in size), engulfed within cellular single-membrane bound organelles, were observed both at the periphery of the larval body, close to the shell, and in the digestive tract (Figure 2C-D; EDS spectra are reported in the SI). NPs were also detected inside the shell's structure using EDS (picture and EDS spectra in the SI).

3.2 Oxidative stress response

The results of the toxicological screening (Figures 3-5) showed that only ZnO NPs were able to trigger oxidative stress *in vivo* under realistic seawater conditions, leading to severe toxicological disruption. In contrast, the samples exposed to MnO_2 and CeO_2 NPs showed no significant effects for all oxidative stress related responses. The only significant difference from the control was a slight downregulation of metallothionein gene expression in the larvae exposed to 500 μM MnO_2 (Figure 3).

The ZnO NPs activated the oxidative stress response machinery from the lowest concentration (i.e. 0.5 uM); signs of oxidative stress were observed at all tiers of the *hierarchical oxidative stress* pathway, although the selected endpoints showed different sensitivies (Figures 3-5).

Overall, the toxicity indicated at the genomic and cellular level was consistent with the significant embryotoxicity recorded in all ZnO NP treatments. All embryos exposed to 5, 50 and 500 uM ZnO NPs failed to reach the D-shaped larvae stage at 26 hpf. On the contrary, regular embryogenesis and larval development was observed in MnO_2 and CeO_2 NPs exposed organisms.

3.3 NP behaviour in the exposure environment

3.3.1 Dissolution

The dissolution experiment carried out with DIW showed that the dissolution model NPs, ZnO NPs, released 3.1% of its zinc content into the ionic form over 24 h. In contrast, almost insignificant dissolution was obtained for MnO_2 and CeO_2 NPs in DIW (0.003% and 0.01%, respectively), consistent with the rationale of the experimental design. The dissolution of ZnO NPs increased in ASW, with 6.7% of zinc released into its ionic form over 24 h.

3.3.2 NP surface reactivity

The results of the cyt c oxidation assay (Figure 6) confirmed the ability of MnO_2 NPs to oxidize the hemeprotein via direct electron transfer, consistent with the bandgap paradigm. Figure 6A shows that the concentration of the reduced cyt c decreased over time due to its oxidation by MnO_2 NPs dispersed in DIW. This pattern was recorded only for the bandgap model NP (i.e.

MnO$_2$ NP), and not for ZnO and CeO$_2$ (results reported in the SI). These results were consistent with the bandgap energy levels computed for the test MOx NPs by Burello and Worth (2011) (Burello and Worth, 2011b) and with evidence from similar experimental screenings reported elsewhere (Zhang *et al.*, 2012).

Changes to the surface reactivity of MnO$_2$ NPs driven by seawater were assessed by comparing this result with that obtained by carrying out the assay with MnO$_2$ NPs dispersed in ASW. Figure 6B shows that MnO$_2$ NPs almost completely lost the ability to oxidize the cellular redox targets once dispersed in seawater. The effective oxidation of the cyt c by the Cu^{2+} solutions in ASW (i.e. positive control) ruled out the hypothesis that this was due to an artefact of the ASW medium.

The results of the plasmid relaxation assay (Figure 7) showed that all test NPs could produce ROS via reactions with H$_2$O$_2$ (i.e. Fenton-like reaction, catalytic decomposition (Lousada *et al.*, 2012)). In fact, in all DIW experiments, the presence of bands corresponding to the linear and circular (uncoiled) DNA confirmed the ability of the tested transitional metal oxide NPs to produce ROS via reactions with H$_2$O$_2$ and to cause single and double strand breaks in the plasmid DNA. However, when dispersed in ASW, only MnO$_2$ NPs did not generate any linear or circular DNA bands.

3.3.3 **Hydrodynamic diameter**

The hydrodynamic size achieved by NP aggregates, once dispersed in ASW, was different for the three test materials. The nearly spherical CeO$_2$ NPs, which showed a homogenous primary size distribution (10-20 nm), formed the largest aggregates in ASW (331.6 ± 12.8 nm); in contrast MnO$_2$ NPs, with a more irregular distribution in terms of aspect ratio under pristine conditions (Table S1 of the SI), formed the smallest aggregates (185.6 ± 8.5 nm). An intermediate size was recorded for ZnO NPs (267.4 ± 18.7 nm; primary size: 20-50 nm).

4 Discussion

Our aim here was to explore the validity of dissolution and bandgap paradigms for predicting NP toxicity *in vivo* and under conditions typical of the marine environment, using oyster embryo-larvae as the model organism, *hierarchical oxidative stress* as a primary toxic pathway, and arrested development of embryos into D-shaped shell larvae as the main pathological outcome. Our results confirm that ZnO NPs triggered oxidative stress *in vivo* under realistic seawater conditions, supporting the paradigm that dissolution can be used to

predict toxicity. In contrast, quenching of the surface reacitvity of MnO_2 NPs restricted the predictive ability of the bandgap paradigm *in vivo* and under seawater conditions.

The increasing production and use of engineered nanomaterials makes testing their safety for humans and the environment a mandatory legislative task (Wacker *et al.*, 2016). Assessing the toxicity of NPs *in vitro* is the first fundamental step which allows for the initial screening of their toxicological potential. However, for those NPs showing high potential for risk, it is crucial to test their hazard under *in vivo* approaches, to test more realistic exposures that are expected to influence the reactivity and bioaccumulation of NPs.

The effective delivery of NPs into the organism and cell is often the first stumbling block, especially for non-dissolving NPs, sealing their toxicological fate in *in vivo* exposures. This is particularly sensitive to marine-like conditions, where the adsorption of seawater ions on the surface of NPs reduces their electrostatic repulsion and promotes aggregation. In this study, ingestion proved to be a feasible NP uptake route for oyster larvae and the size of NP aggregates in ASW turned out to be compatible with the larvae' particle filtration and sorting system. Although the extent of NP cellular internalization was small compared to the overall amount ingested, the TEM-EDS results proved that ingested NPs were not prevented from crossing the organisms' external barriers and entering cells during the early larval stages. The presence of single particles inside endosomes of the digestive tract cells supports endocytosis as a major internalization pathway for ingested NPs (Koehler *et al.*, 2008, García-Alonso *et al.*, 2011). This mechanism has been studied extensively *in vitro* (Sakhtianchi *et al.*, 2013), and images of endocytosed NPs from *in vivo* experiments have been reported for other aquatic organisms (García-Alonso *et al.*, 2011, Marchesano *et al.*, 2013), but not previously for oyster embryos.

Cellular structures densely packed with NPs, like those observed in the present study (Figure 2C-D), have been reported in both *in vitro* and *in vivo* studies focusing on NP cellular trafficking (Krpetić *et al.*, 2011, Marchesano *et al.*, 2013). At the end of the endocytocytic pathway, lysosome-like bodies highly packed with NPs can be formed as final storage compartments, to keep foreign material sealed inside cells and be discharged via exocytosis (Marchesano *et al.*, 2013). The presence of these bodies outside of the digestive organs, i.e. inside peripheral cells, may suggest NP translocation or that some forms of NP cellular penetration could have occurred before the formation of a functional filtration-digestive apparatus, i.e. during embryogenesis, when organisms are not sheltered by shells and NPs can attach themselves to the body surface. Skin penetration by NPs (i.e. via endocytosis or direct membrane uptake) has been observed in embryo-early larval stages of fish (Japanese medaka (Lee *et al.*, 2014), zebrafish (Asharani *et al.*, 2008, Muth-Köhne *et al.*, 2013)) and in unshelled invertebrate organisms (the freshwater polyp *Hydra vulgaris* (Marchesano *et al.*, 2013)).

We show that ZnO NPs can trigger oxidative stress *in vivo* under realistic seawater conditions, leading to severe toxicological disruption. Zn could have been taken up by oyster embryo-larvae both in its ionic and particulate forms, and ZnO NP dissolution could have occurred in the water, in the digestive organs or inside cells. The different bioaccumulation routes of both ZnO nanoparticles and shed Zn^{2+} ions have been extensively studied through *in vitro* and *in vivo* models (Ma *et al.*, 2013, Liu *et al.*, 2016). Zn^{2+} is an essential element and, at the cell membrane, its internalization is through carrier mediated metal ion transporters, either specific transporters or those primarily used for other essential metals. Although the toxic role of the metal ions released in the exposure medium is well documented, ZnO NP toxicity may be further mediated by the nanoparticle form (Poynton *et al.*, 2011, Bacchetta *et al.*, 2014). The activation of oxidative stress by ZnO NPs is suggested to be the main toxicity pathway. Cytotoxic effects typically recorded *in vitro* are mitochondria dysfunction, endoplasmatic reticulum stress, intracellular Ca^{2+} flux, lysosomal disruption and inflammatory response up to cell death (Liu *et al.*, 2016). Similar to the present study, the most frequent *in vivo* effects in aquatic organisms are the expression of genes involved in oxidative stress responses, changes in the stress-related biochemical parameters, increased lipid peroxidation and enhanced cell membrane permeability (Poynton *et al.*, 2011, Bacchetta *et al.*, 2014, Minetto *et al.*, 2016).

In the case of MnO_2 NPs, the bandgap paradigm was not adhered to under marine conditions. The abiotic tests consistently highlighted that the surface oxidation potential of MnO_2 NPs was quenched by seawater and hence the bandgap paradigm, in which the overlap of conduction band with cellular redox potential enables the oxidation of cellular components and the generation of ROS, did not hold. Mn oxides are powerful oxidants with a multi-step activation mechanism consisting of: 1) diffusion of the reductant into the boundary layer, 2) formation of a surface complex between the adsorbate and the oxide's active sites, and 3) electron transfer from the reductant to the oxide surface. The second step is considered an important reaction rate limiting stage, highly sensitive to the chemical composition of the medium (Remucal and Ginder-Vogel, 2014). In the particular case of seawater conditions, the interaction with ions could decrease or prevent NP redox activity by 1) blocking the active sites of the minerals' surface via complexation, 2) screening the surface via ion adsorption and preventing the interaction with organic reductants, and 3) decreasing the average oxidation state of the oxide.

Although the third hypothesis (i.e. change of Mn oxidation state) cannot be excluded without further evidence, this seems weaker compared to the complexation-adsorption hypotheses (i.e. first and second hypotheses). In natural environments Mn occurs in three oxidation states (i.e. Mn^{2+}, Mn^{3+}, Mn^{4+}) which can exchange through oxidation/reducing cycles involving both biotic and abiotic processes. This dynamic redox cycling tends to occur across redox transition

zones, such as subsurface environments including oxic-anoxic boundaries in soil and sediment, suboxic water column, and acid mine drainage areas. Thus, in oxygenated marine waters, Mn^{4+} oxide minerals, including colloids, represent one of the main forms of manganese together with Mn^{3+} oxyhydroxides (Post, 1999, Anschutz *et al.*, 2005); these Mn^{3+}/Mn^{4+} oxides minerals can be reduced to Mn^{2+} under very reducing conditions, such as those typical of deep sediments (Hem, 1978, Anschutz *et al.*, 2005). Considering this picture, under the oxic conditions tested in the present experiment, a sharp change of Mn oxidation state seemed unlikely. Furthermore, a partial decrease of the average oxidation state of Mn due to the reduction of Mn^{4+} to Mn^{3+} cannot fully explain the lack of oxidation capacity of MnO_2 NPs pointed out by the abiotic screening in ASW. In spite of the chemical formula, both natural and synthesized $Mn^{4+}O_2$ minerals commonly contain variable trace/amounts of Mn^{3+} in their structure (Remucal and Ginder-Vogel, 2014). It is also of relevance to consider that also Mn^{3+} oxide and Mn^{3+}/Mn^{2+} oxide minerals show high oxidation capacity (Remucal and Ginder-Vogel, 2014); consistently, Mn_2O_3 was one of the MOx NPs showing the highest oxidation potential via the bandgap mechanism as described by Zhang and collaborators (Zhang *et al.*, 2012).

In contrast, the hypotheses of adsorption-complexation are supported by the extraordinary sorption capacity of Mn oxide minerals, including colloids. Mn oxide minerals are important natural adsorbents in aquatic environments, for instance as a solid phase controlling the concentrations of certain metals in natural waters (Hem, 1978, Balistrieri and Murray, 1982, Kanungo and Mahapatra, 1989, Feng *et al.*, 1999, Post, 1999). There is large agreement that this property is due to the low pH at the isoelectric point (pH_{IEP}) and strong acid sites that are a feature of Mn oxide minerals (Feng *et al.*, 2007). Microscopic characterization of the structures forming at the solid-liquid interface (i.e. via Extended X-ray Absorption Fine Structure Spectroscopy, EXAFS) have highlighted the importance of crystallographic structure for the sorption potential of manganese oxide mineral phases (e.g. vacancy sites, surface microstructures) (Li *et al.*, 2004, Pan *et al.*, 2004).

The sorption capacity of different Mn oxide phases has been studied in relation to several metal ions (Li *et al.*, 2004, Pan *et al.*, 2004, Tripathy and Kanungo, 2005, Feng *et al.*, 2007, Wang and Giammar, 2015). In some cases the adsorption has been described as irreversible (e.g. adsorption of Zn^{2+} ions on γ-MnO_2 (Pan *et al.*, 2004)) and has been related to the passivation of the surface reactivity (Wang and Giammar, 2015). Regarding the adsorption of seawater ions on the surface of Mn oxide, the nature of this specific interaction was studied by Balistrieri and Murray (1982) according to the metal oxide surface complexation model (Stumm, 1993). They found that the association of cations on the surface of one of the most abundant mineral phases of MnO_2 in the marine environment (i.e. δ-MnO_2) was slightly

stronger than a simple electrostatic interaction, suggesting the formation of bi- and mono-dentate complexes with di- and mono-valent seawater cations.

The nature of the interaction between seawater ions and the surface of the three test NPs (i.e. physico-sorption vs chemico-sorption; reversibility, etc) could explain the results of the plasmid relaxation assay. The pH_{IEP} values of the three test NPs (i.e. 4.8, 7.9, 10.4 for MnO_2 NPs, CeO_2 NPs, and ZnO NPs, respectively; more details in the SI) suggest different modes of interaction with seawater ions. In particular, MnO_2 NPs, with lower pH_{IEP} values, are expected to have a higher adsorption capacity for seawater cations at the pH of ASW (i.e. 8.10 ± 0.05). This would have led to a strong adsorption of seawater cations on the surface of MnO_2 NPs, preventing H_2O_2 from contacting surface reactive sites and generate ROS (Figure 8). In support of this notion, the adsorption of seawater cations was found to impair the overall sorption capacity of Mn oxide minerals for certain metals (i.e via a sorption competition mechanism) (Tripathy and Kanungo, 2005).

Further investigation is needed to better understand the nature and strength of the interaction between seawater ions and the surface of reactive NPs and the consequences for their overall oxidation potential. Structural proprieties of MOx NPs which can predict the quenching of their intrinsic reactivity by seawater ions (i.e. pH_{IEP}, adsorption capacity) could be additional factors to consider when predicting the toxicity of MOx NPs in the marine environment. These variables could be used to adjust the toxicological predictions based on general structure-activity paradigms (e.g. bandgap) to realistic environmental scenarios.

However, the quenching of MnO_2 NP oxidation potential by seawater cations may not have been the only factor causing the complete lack of toxicity in the larvae exposed to MnO_2 NPs, which showed high ingestion of NPs and signs of cellular internalization of NPs. Once ingested, the NPs move through a sequence of biological environments, featuring a wide range of pH values, which may modify the equilibrium adsorption and thus the reactivity. The confinement of internalized NPs inside cellular storage compartments, their possible exocytosis, and further surface passivation through specific cellular processes (i.e. protein corona formation) may all have been factors contributing to the lack of toxicity recorded in our *in vivo* study. Under the hypothesis that CeO_2 NPs were internalized into cells, as observed for MnO_2 NPs, these possible mechanisms, which oyster embryo-larvae have evolved to specifically cope with the bioaccumulation of mineral particles, can help to explain the toxicological stasis recorded for CeO_2 NPs. Indeed previous characterization of CeO_2 surface reactivity in seawater discounted drastic surface passivation via both cation adsorption and the reduction of the density of Ce^{3+} active sites (Dogra *et al.*, 2016). Nevertheless, the toxicological behavior of CeO_2 is controversial and still the subject of research. CeO_2 NPs are noted to act as pro-oxidant and as anti-oxidant/radical scavengers, depending on dose and

reaction system (Gagnon and Fromm, 2015) and so CeO_2 behavior as a SOD-mimicking agent under the conditions achieved in the present *in vivo* exposure cannot be excluded.

5   Conclusions

We present evidence showing the effectiveness of dissolution and *hierarchical oxidative stress* paradigms to predict the toxicity of metal oxide NPs in the marine environment. ZnO NPs, which can release Zn^{2+} in seawater and in biological environments, induced oxidative stress in oyster embryo-larvae, which were exposed to ZnO NPs for 24 h at increasing concentrations. In contrast, the validity of the bandgap paradigm was challenged by seawater driven changes to the MnO_2 NP particles' surface reactivity. In this regard, the quenching of the intrinsic reactivity of NPs due to the adsorption-complexation of seawater ions on their surface active sites is a hypothesis deserving of further attention. The strength/nature of counterion adsorption could be an important factor to consider in establishing the potential toxicological risk of non-dissolving MOx NPs in the marine environment.

Finally, this study indicated the need to address the biological-cellular systems which can manage the storage-disposal of solid particles bioaccumulated by organisms. Filter feeding larvae and other aquatic organisms living in environments enriched in suspended mineral colloids have evolved to cope with the bioaccumulation of natural nanoparticles, which may now play a role in dealing with the environmental contamination by engineered NPs.

Supporting Information Available

The following material is available in the Supporting Information: primary physico-chemical properties of the test NPs; primer sequences, qPCR conditions and performance; TEM-EDS study of biological fate of MnO_2 NPs; methods for the characterization of the behaviour of the test NPs; results of the cytochrome c oxidation assay carried out on ZnO and CeO_2 NP dispersions in deionized water.

Disclosure statement

The authors report no conflicts of interest.

References

Anschutz, P., Dedieu, K., Desmazes, F. & Chaillou, G., 2005. Speciation, oxidation state, and reactivity of particulate manganese in marine sediments. *Chemical Geology,* 218**,** 265-279.

Asharani, P.V., Yi Lian, W., Zhiyuan, G. & Suresh, V., 2008. Toxicity of silver nanoparticles in zebrafish models. *Nanotechnology,* 19**,** 255102.

Bacchetta, R., Moschini, E., Santo, N., Fascio, U., Del Giacco, L., Freddi, S., Camatini, M. & Mantecca, P., 2014. Evidence and uptake routes for Zinc oxide nanoparticles through the gastrointestinal barrier in Xenopus laevis. *Nanotoxicology,* 8**,** 728-744.

Balistrieri, L.S. & Murray, J.W., 1982. THE SURFACE-CHEMISTRY OF DELTA-MNO2 IN MAJOR ION SEA-WATER. *Geochimica Et Cosmochimica Acta,* 46**,** 1041-1052.

Burello, E. & Worth, A.P., 2011a. QSAR modeling of nanomaterials. *Wiley Interdisciplinary Reviews: Nanomedicine and Nanobiotechnology,* 3**,** 298-306.

Burello, E. & Worth, A.P., 2011b. A theoretical framework for predicting the oxidative stress potential of oxide nanoparticles. *Nanotoxicology,* 5**,** 228-235.

Camejo, G., Wallin, B. & Enojärvi, M., 1998. Analysis of Oxidation and Antioxidants Using Microtiter Plates. *In* D. Armstrong (ed.) *Free Radical and Antioxidant Protocols.* Totowa, NJ: Humana Press, 377-387.

Collin, B., Auffan, M., Johnson, A.C., Kaur, I., Keller, A.A., Lazareva, A., Lead, J.R., Ma, X., Merrifield, R.C., Svendsen, C., White, J.C. & Unrine, J.M., 2014. Environmental release, fate and ecotoxicological effects of manufactured ceria nanomaterials. *Environmental Science: Nano,* 1**,** 533-548.

Delaval, M., Wohlleben, W., Landsiedel, R., Baeza-Squiban, A. & Boland, S., 2017. Assessment of the oxidative potential of nanoparticles by the cytochrome c assay: assay improvement and development of a high-throughput method to predict the toxicity of nanoparticles. *Archives of Toxicology,* 91**,** 163-177.

Dogra, Y., Arkill, K.P., Elgy, C., Stolpe, B., Lead, J., Valsami-Jones, E., Tyler, C.R. & Galloway, T.S., 2016. Cerium oxide nanoparticles induce oxidative stress in the sediment-dwelling amphipod Corophium volutator. *Nanotoxicology,* 10**,** 480-487.

Feng, Q., Kanoh, H. & Ooi, K., 1999. Manganese oxide porous crystals. *Journal of Materials Chemistry,* 9**,** 319-333.

Feng, X.H., Zhai, L.M., Tan, W.F., Liu, F. & He, J.Z., 2007. Adsorption and redox reactions of heavy metals on synthesized Mn oxide minerals. *Environmental Pollution,* 147**,** 366-373.

Ferraro, D., Tredici, I.G., Ghigna, P., Castillo-Michel, H., Falqui, A., Di Benedetto, C., Alberti, G., Ricci, V., Anselmi-Tamburini, U. & Sommi, P., 2017. Correction: Dependence of the Ce(iii)/Ce(iv) ratio on intracellular localization in ceria nanoparticles internalized by human cells. *Nanoscale,* 9**,** 5021-5021.

Gagnon, J. & Fromm, K.M., 2015. Toxicity and Protective Effects of Cerium Oxide Nanoparticles (Nanoceria) Depending on Their Preparation Method, Particle Size, Cell Type, and Exposure Route. *European Journal of Inorganic Chemistry,* 2015**,** 4510-4517.

García-Alonso, J., Khan, F.R., Misra, S.K., Turmaine, M., Smith, B.D., Rainbow, P.S., Luoma, S.N. & Valsami-Jones, E., 2011. Cellular Internalization of Silver Nanoparticles in Gut Epithelia of the Estuarine Polychaete Nereis diversicolor. *Environmental Science & Technology,* 45**,** 4630-4636.

Genard, B., Miner, P., Nicolas, J.-L., Moraga, D., Boudry, P., Pernet, F. & Tremblay, R., 2013. Integrative Study of Physiological Changes Associated with Bacterial Infection in Pacific Oyster Larvae. *PLOS ONE,* 8**,** e64534.

Guo, X., He, Y., Zhang, L., Lelong, C. & Jouaux, A., 2015. Immune and stress responses in oysters with insights on adaptation. *Fish & Shellfish Immunology,* 46**,** 107-119.

He, X., Aker, W.G., Fu, P.P. & Hwang, H.-M., 2015. Toxicity of engineered metal oxide nanomaterials mediated by nano-bio-eco-interactions: a review and perspective. *Environmental Science: Nano,* 2**,** 564-582.

Hem, J.D., 1978. Redox processes at surfaces of manganese oxide and their effects on aqueous metal ions. *Chemical Geology,* 21**,** 199-218.

Joo, S.H. & Zhao, D., 2017. Environmental dynamics of metal oxide nanoparticles in heterogeneous systems: A review. *Journal of Hazardous Materials,* 322, Part A**,** 29-47.

Jrc64075, 2011. NM-Series of Representative Manufactured Nanomaterials - Zinc Oxide NM-110, NM-111, NM-112, NM-113: Characterisation and Test Item Preparation. Publications Office of the European Union.

Jrc89825, 2014. Cerium Dioxide, NM-211, NM-212, NM-213. Characterisation and test item preparation. Publications Office of the European Union.

Kanungo, S.B. & Mahapatra, D.M., 1989. Interfacial properties of some hydrous manganese dioxides in 1-1 electrolyte solution. *Journal of Colloid and Interface Science,* 131**,** 103-111.

Kaweeteerawat, C., Ivask, A., Liu, R., Zhang, H., Chang, C.H., Low-Kam, C., Fischer, H., Ji, Z., Pokhrel, S., Cohen, Y., Telesca, D., Zink, J., Mädler, L., Holden, P.A., Nel, A. & Godwin, H., 2015. Toxicity of Metal Oxide Nanoparticles in Escherichia coli Correlates with Conduction Band and Hydration Energies. *Environmental Science & Technology,* 49**,** 1105-1112.

Klaine, S.J., Alvarez, P.J.J., Batley, G.E., Fernandes, T.F., Handy, R.D., Lyon, D.Y., Mahendra, S., Mclaughlin, M.J. & Lead, J.R., 2008. Nanomaterials in the environment: Behavior, fate, bioavailability, and effects. *Environmental Toxicology and Chemistry,* 27**,** 1825-1851.

Koehler, A., Marx, U., Broeg, K., Bahns, S. & Bressling, J., 2008. Effects of nanoparticles in Mytilus edulis gills and hepatopancreas – A new threat to marine life? *Marine Environmental Research,* 66**,** 12-14.

Krpetić, Ž., Saleemi, S., Prior, I.A., Sée, V., Qureshi, R. & Brust, M., 2011. Negotiation of Intracellular Membrane Barriers by TAT-Modified Gold Nanoparticles. *ACS Nano,* 5**,** 5195-5201.

Lee, B.C., Kim, J., Cho, J.G., Lee, J.W., Duong, C.N., Bae, E., Yi, J., Eom, I.C., Choi, K., Kim, P. & Yoon, J., 2014. Effects of ionization on the toxicity of silver nanoparticles to Japanese medaka (Oryzias latipes) embryos. *Journal of Environmental Science and Health Part a-Toxic/Hazardous Substances & Environmental Engineering,* 49**,** 287-293.

Leverett D, T.J., 2013. Oyster embryo-larval bioassay (Revised). ICES Techniques in Marine Environmental Sciences No 54, 34 pp.

Li, J., Zhang, Y., Xiang, Z., Xiao, S., Yu, F. & Yu, Z., 2013. High mobility group box 1 can enhance NF-κB activation and act as a pro-inflammatory molecule in the Pacific oyster, Crassostrea gigas. *Fish & Shellfish Immunology,* 35**,** 63-70.

Li, X., Pan, G., Qin, Y., Hu, T., Wu, Z. & Xie, Y., 2004. EXAFS studies on adsorption–desorption reversibility at manganese oxide–water interfaces. *Journal of Colloid and Interface Science,* 271**,** 35-40.

Liu, J., Feng, X., Wei, L., Chen, L., Song, B. & Shao, L., 2016. The toxicology of ion-shedding zinc oxide nanoparticles. *Critical Reviews in Toxicology,* 46**,** 348-384.

Liu, R., Zhang, H.Y., Ji, Z.X., Rallo, R., Xia, T., Chang, C.H., Nel, A. & Cohen, Y., 2013. Development of structure-activity relationship for metal oxide nanoparticles. *Nanoscale,* 5**,** 5644-5653.

Lousada, C.M., Johansson, A.J., Brinck, T. & Jonsson, M., 2012. Mechanism of H2O2 Decomposition on Transition Metal Oxide Surfaces. *The Journal of Physical Chemistry C,* 116**,** 9533-9543.

Ma, H., Williams, P.L. & Diamond, S.A., 2013. Ecotoxicity of manufactured ZnO nanoparticles – A review. *Environmental Pollution,* 172**,** 76-85.

Mai, H., Gonzalez, P., Pardon, P., Tapie, N., Budzinski, H., Cachot, J. & Morin, B., 2014. Comparative responses of sperm cells and embryos of Pacific oyster (Crassostrea gigas) to exposure to metolachlor and its degradation products. *Aquatic Toxicology,* 147**,** 48-56.

Marchesano, V., Hernandez, Y., Salvenmoser, W., Ambrosone, A., Tino, A., Hobmayer, B., M De La Fuente, J. & Tortiglione, C., 2013. Imaging Inward and Outward Trafficking of Gold Nanoparticles in Whole Animals. *ACS Nano,* 7**,** 2431-2442.

Mazzolini, J., Weber, R.J.M., Chen, H.-S., Khan, A., Guggenheim, E., Shaw, R.K., Chipman, J.K., Viant, M.R. & Rappoport, J.Z., 2016. Protein Corona Modulates Uptake and Toxicity of Nanoceria via Clathrin-Mediated Endocytosis. *The Biological Bulletin,* 231**,** 40-60.

Meng, H., Xia, T., George, S. & Nel, A.E., 2009. A Predictive Toxicological Paradigm for the Safety Assessment of Nanomaterials. *ACS Nano,* 3**,** 1620-1627.

Minetto, D., Volpi Ghirardini, A. & Libralato, G., 2016. Saltwater ecotoxicology of Ag, Au, CuO, TiO2, ZnO and C60 engineered nanoparticles: An overview. *Environment International,* 92**,** 189-201.

Montagnani, C., Kappler, C., Reichhart, J.M. & Escoubas, J.M., 2004. Cg-Rel, the first Rel/NF-kappa B homolog characterized in a mollusk, the Pacific oyster Crassostrea gigas. *Febs Letters,* 561**,** 75-82.

Muth-Köhne, E., Sonnack, L., Schlich, K., Hischen, F., Baumgartner, W., Hund-Rinke, K., Schäfers, C. & Fenske, M., 2013. The toxicity of silver nanoparticles to zebrafish embryos increases through sewage treatment processes. *Ecotoxicology,* 22**,** 1264-1277.

Nel, A., Xia, T., Mädler, L. & Li, N., 2006. Toxic Potential of Materials at the Nanolevel. *Science,* 311**,** 622-627.

Nelson, B., Johnson, M., Walker, M., Riley, K. & Sims, C., 2016. Antioxidant Cerium Oxide Nanoparticles in Biology and Medicine. *Antioxidants*, 5**,** 15.

Pan, G., Qin, Y., Li, X., Hu, T., Wu, Z. & Xie, Y., 2004. EXAFS studies on adsorption–desorption reversibility at manganese oxides–water interfaces. *Journal of Colloid and Interface Science,* 271**,** 28-34.

Plascencia-Villa, G., Starr, C.R., Armstrong, L.S., Ponce, A. & Jose-Yacaman, M., 2012. Imaging interactions of metal oxide nanoparticles with macrophage cells by ultra-high resolution scanning electron microscopy techniques. *Integrative Biology,* 4**,** 1358-1366.

Post, J.E., 1999. Manganese oxide minerals: crystal structures and economic and environmental significance. *Proc Natl Acad Sci U S A,* 96**,** 3447-54.

Poynton, H.C., Lazorchak, J.M., Impellitteri, C.A., Smith, M.E., Rogers, K., Patra, M., Hammer, K.A., Allen, H.J. & Vulpe, C.D., 2011. Differential Gene Expression in Daphnia magna Suggests Distinct Modes of Action and Bioavailability for ZnO Nanoparticles and Zn Ions. *Environmental Science & Technology,* 45**,** 762-768.

Remucal, C.K. & Ginder-Vogel, M., 2014. A critical review of the reactivity of manganese oxides with organic contaminants. *Environmental Science: Processes & Impacts,* 16**,** 1247-1266.

Sakhtianchi, R., Minchin, R.F., Lee, K.-B., Alkilany, A.M., Serpooshan, V. & Mahmoudi, M., 2013. Exocytosis of nanoparticles from cells: Role in cellular retention and toxicity. *Advances in Colloid and Interface Science,* 201–202**,** 18-29.

Song, X., Wang, H., Xin, L., Xu, J., Jia, Z., Wang, L. & Song, L., 2016. The immunological capacity in the larvae of Pacific oyster Crassostrea gigas. *Fish & Shellfish Immunology,* 49**,** 461-469.

Stumm, W., 1993. Aquatic colloids as chemical reactants: surface structure and reactivity. *Colloids and Surfaces A: Physicochemical and Engineering Aspects,* 73**,** 1-18.

Sussarellu, R., Fabioux, C., Camacho Sanchez, M., Le Goïc, N., Lambert, C., Soudant, P. & Moraga, D., 2012. Molecular and cellular response to short-term oxygen variations in the Pacific oyster Crassostrea gigas. *Journal of Experimental Marine Biology and Ecology,* 412, 87-95.

Tantra, R., Oksel, C., Puzyn, T., Wang, J., Robinson, K.N., Wang, X.Z., Ma, C.Y. & Wilkins, T., 2015. Nano(Q)SAR: Challenges, pitfalls and perspectives. *Nanotoxicology,* 9**,** 636-642.

Tirapé, A., Bacque, C., Brizard, R., Vandenbulcke, F. & Boulo, V., 2007. Expression of immune-related genes in the oyster Crassostrea gigas during ontogenesis. *Developmental & Comparative Immunology,* 31**,** 859-873.

Tripathy, S.S. & Kanungo, S.B., 2005. Adsorption of Co2+, Ni2+, Cu2+ and Zn2+ from 0.5 M NaCl and major ion sea water on a mixture of δ-MnO2 and amorphous FeOOH. *Journal of Colloid and Interface Science,* 284, 30-38.

Vogeler, S., Bean, T.P., Lyons, B.P. & Galloway, T.S., 2016. Dynamics of nuclear receptor gene expression during Pacific oyster development. *BMC Developmental Biology,* 16, 33.

Wacker, M.G., Proykova, A. & Santos, G.M.L., 2016. Dealing with nanosafety around the globe—Regulation vs. innovation. *International Journal of Pharmaceutics,* 509**,** 95-106.

Wang, Z. & Giammar, D.E., 2015. Metal Contaminant Oxidation Mediated by Manganese Redox Cycling in Subsurface Environment. *Advances in the Environmental Biogeochemistry of Manganese Oxides.* American Chemical Society, 29-50.

Xia, T., Kovochich, M., Liong, M., Mädler, L., Gilbert, B., Shi, H., Yeh, J.I., Zink, J.I. & Nel, A.E., 2008. Comparison of the Mechanism of Toxicity of Zinc Oxide and Cerium Oxide Nanoparticles Based on Dissolution and Oxidative Stress Properties. *ACS Nano,* 2**,** 2121-2134.

Zhang, H., Ji, Z., Xia, T., Meng, H., Low-Kam, C., Liu, R., Pokhrel, S., Lin, S., Wang, X., Liao, Y.-P., Wang, M., Li, L., Rallo, R., Damoiseaux, R., Telesca, D., Mädler, L., Cohen, Y., Zink, J.I. & Nel, A.E., 2012. Use of Metal Oxide Nanoparticle Band Gap To Develop a Predictive Paradigm for Oxidative Stress and Acute Pulmonary Inflammation. *ACS Nano,* 6**,** 4349-4368.

Zhang, L., Li, L. & Zhang, G., 2011. Gene discovery, comparative analysis and expression profile reveal the complexity of the Crassostrea gigas apoptosis system. *Developmental & Comparative Immunology,* 35**,** 603-610.

Zhang, Y., Li, J., Yu, F., He, X.C. & Yu, Z.N., 2013. Allograft inflammatory factor-1 stimulates hemocyte immune activation by enhancing phagocytosis and expression of inflammatory cytokines in Crassostrea gigas. *Fish & Shellfish Immunology,* 34**,** 1071-1077.
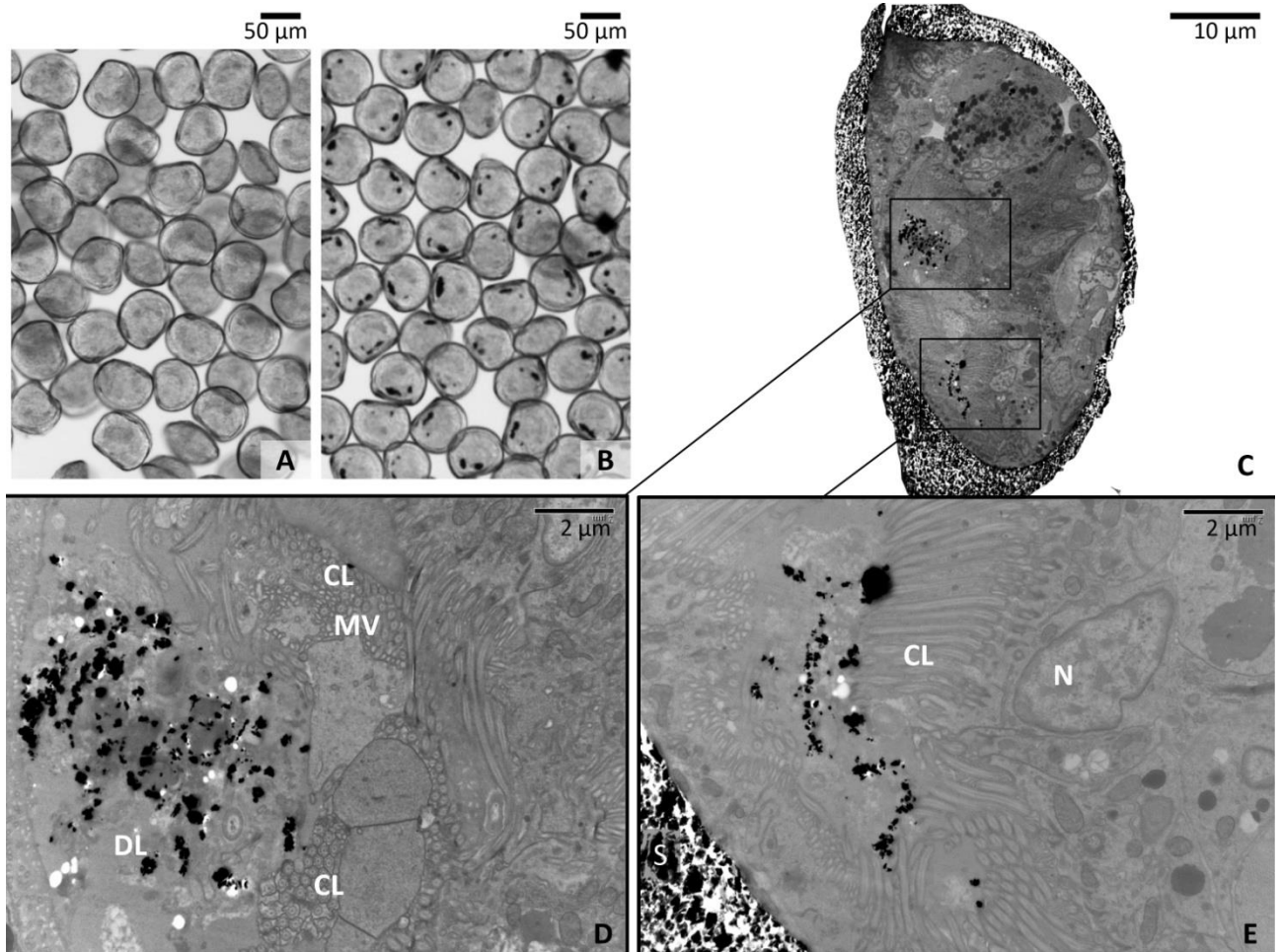
Figures

Figure 1 NP ingestion by *C. gigas* larvae. (A) Light microscope image of D-shaped shell larvae from control. Light microscope (B) and TEM (C) images of D-shaped shell larvae exposed to 500 uM MnO_2 NPs, showing clumps of ingested NPs inside their body. NP aggregates were densely packed inside the digestive tract (D) and among the cilia of the retracted velum (E). Abbreviations: CL, cilia; DL, digestive lumen; MV, microvilli; N, nucleus.
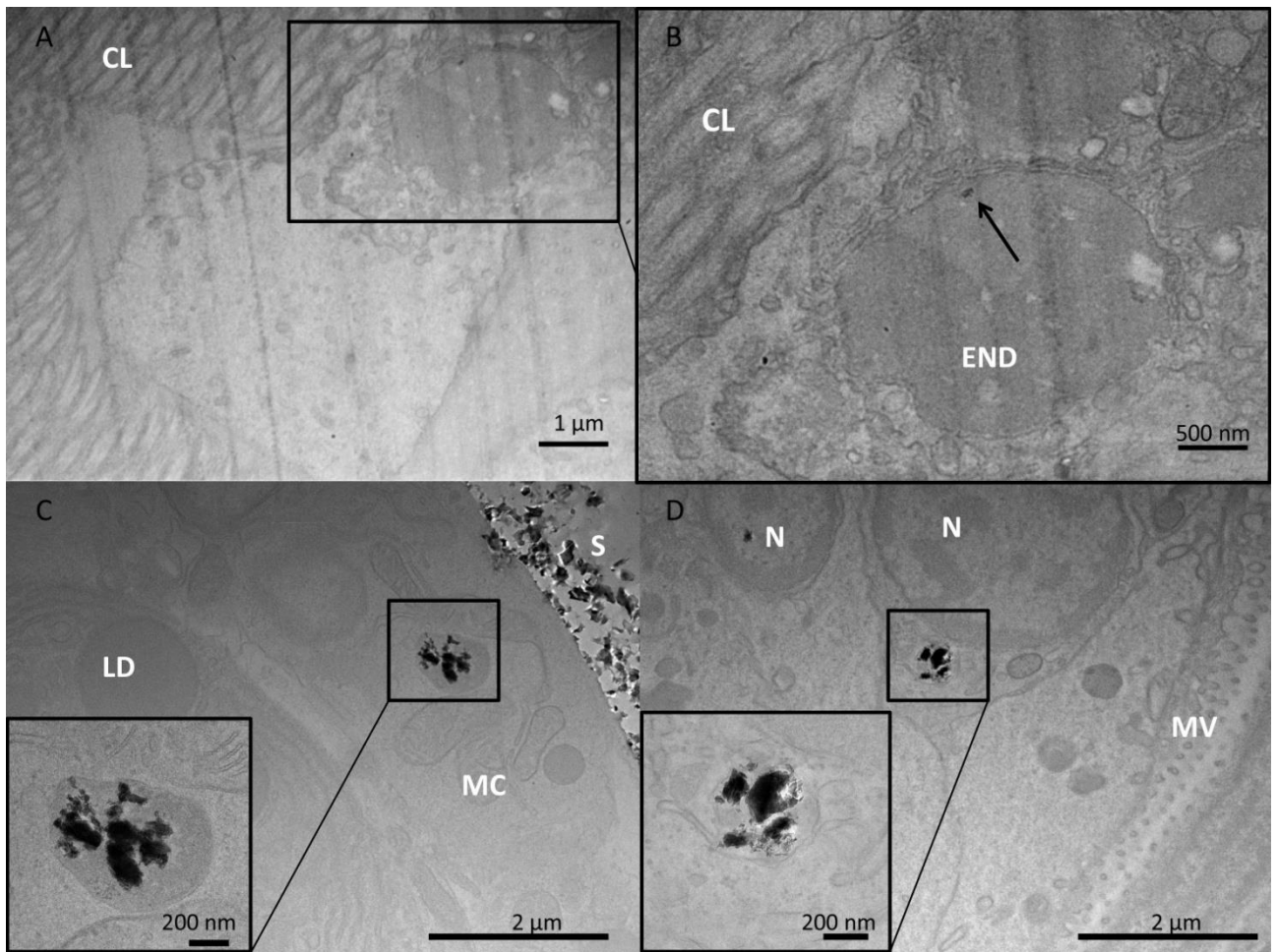
Figure 2 NP cellular internalization (*C. gigas* D-shaped shell larvae exposed to 500 uM MnO$_2$ NPs). A-B) Single NP inside an endosome-like vesicle in the adsorption apparatus. C-D) Highly packed NPs in single-membrane bound organelles of cells close to the shell (C) and in the adsorption organ (D). Abbreviations: CL, cilia; END, endosome-like structure; LD, lipid droplet; MC, mitochondrion; MV, microvilli; N, nucleus.
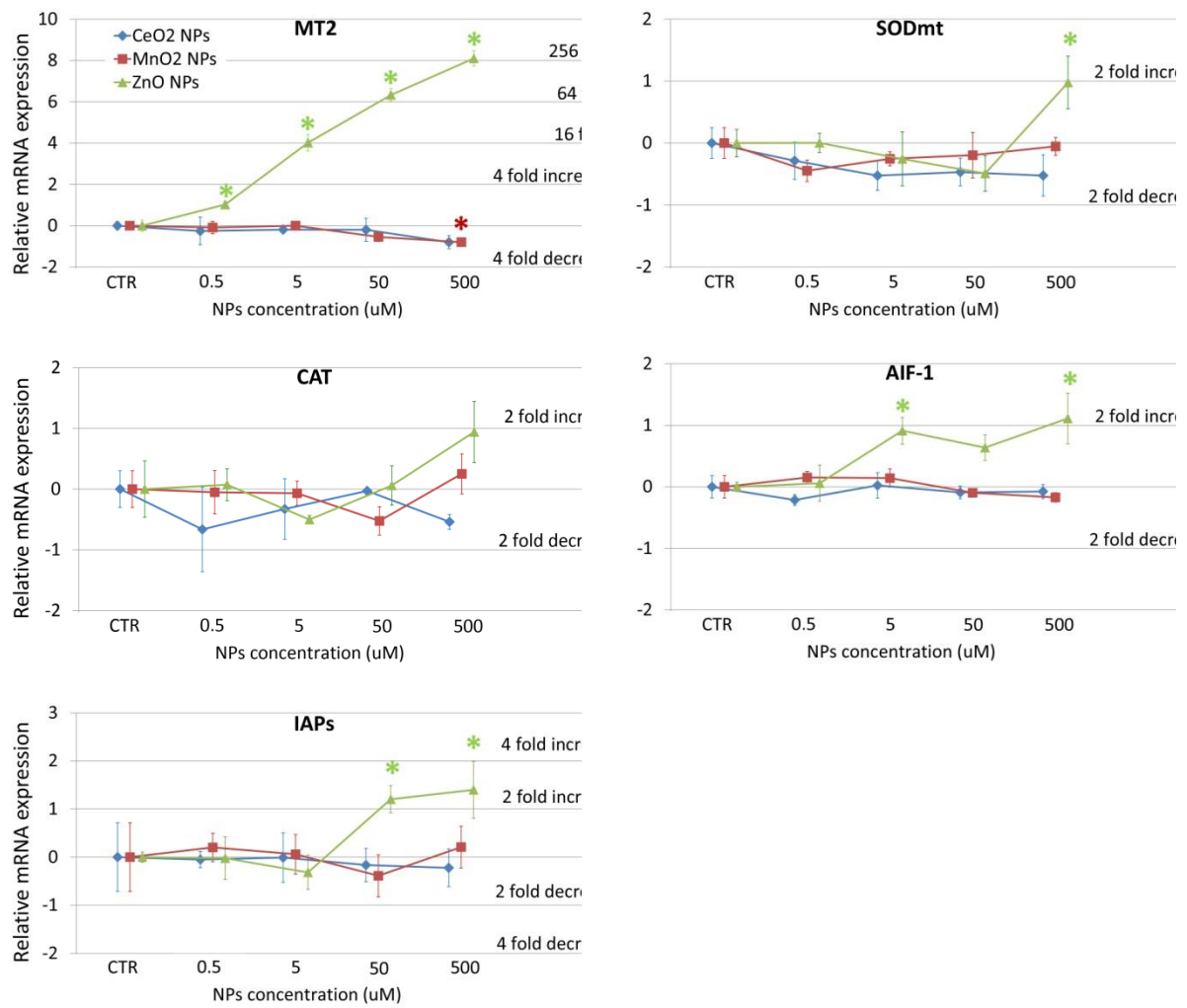
Figure 3 Relative expression of target genes in NP exposed samples compared to the control (log$_2$). (*) marks data that significantly differed from the control (ANOVA one-way, Tukey HDS post-hoc test; n=3, p-value=0.05).
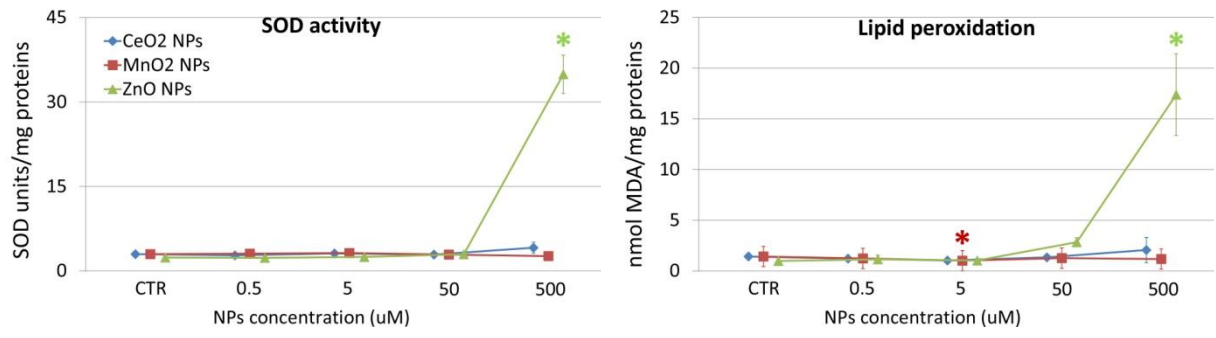
Figure 4 Results of functional assays. SOD activity and lipid peroxidation (TBARS assay) as a function of NP concentration. (*) marks data that significantly differed from the control (ANOVA one-way, Tukey HDS post-hoc test; n=3, p-value=0.05).
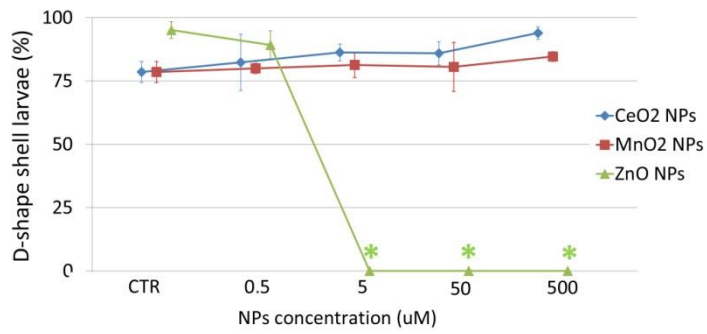
Figure 5 Oyster embryo-larvae bioassay. Percentage of embryos normally developed into D-shaped shell larvae (at 26 hpf) as a function of NP concentration. (*) marks samples that significantly differed from the control (ANOVA one-way, Tukey HDS post-hoc test; n=3, p-value=0.05).
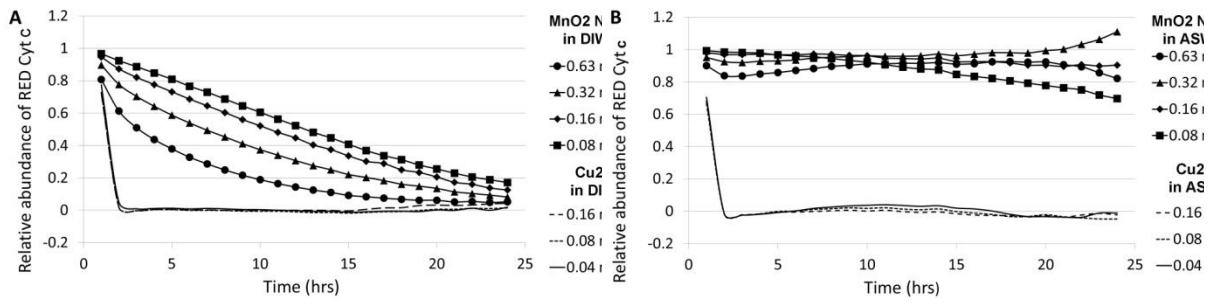
Figure 6 Cytochrome c oxidation assay. Abiotic oxidation of reduced cyt c by MnO₂ NPs dispersed in DIW (A) and in ASW (B) over a 24 h reaction. Cu²⁺ was used as positive control.
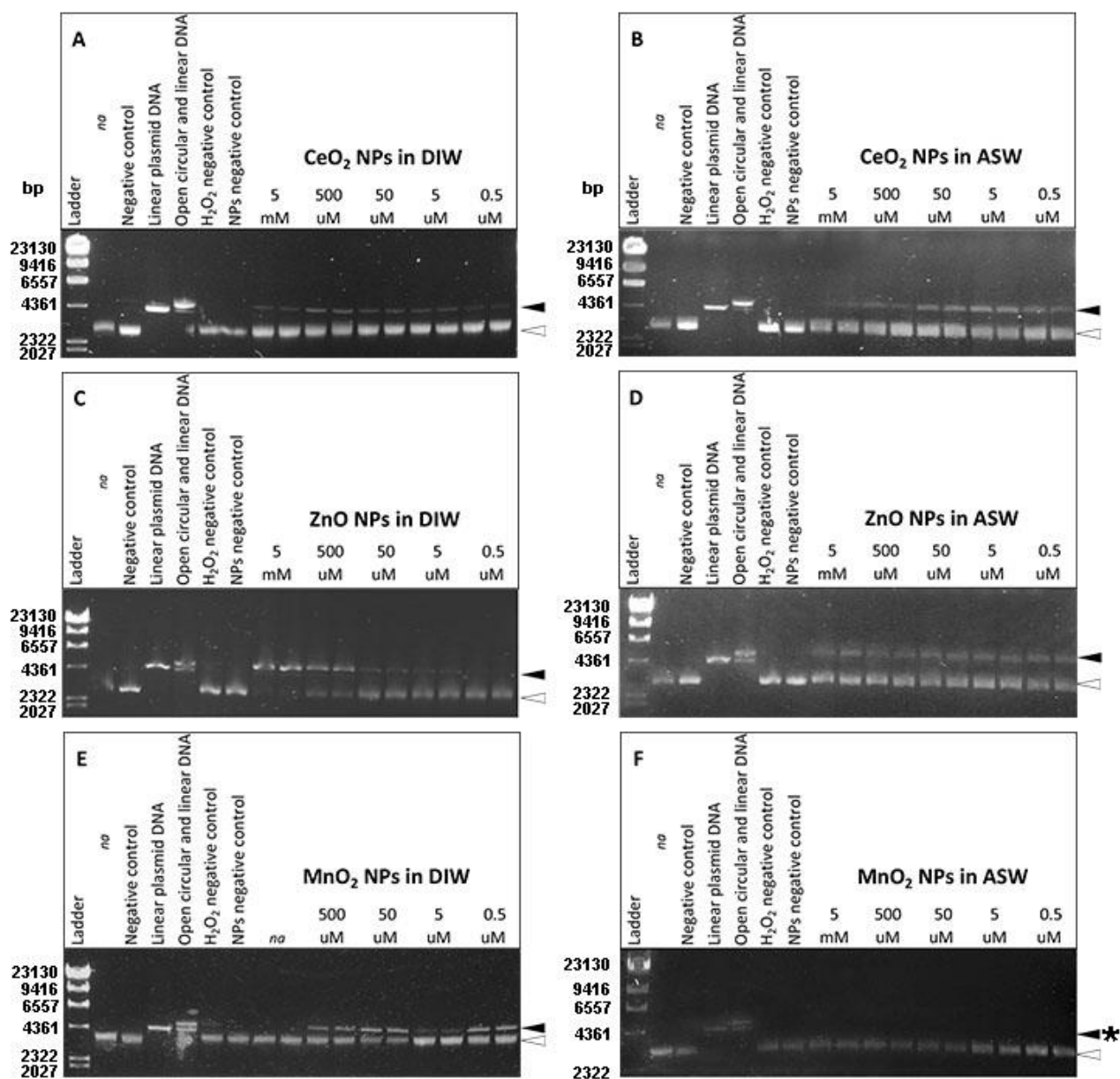
Figure 7 ROS generation via reaction with H_2O_2 in DIW and ASW: Plasmid Relaxation experiments undertaken with CeO_2, ZnO, and MnO_2 NPs. Several positive and negative controls were undertaken together with reaction mixtures containing H_2O_2 and increasing concentrations of the test NPs. In order (from the left to the right): DNA ladder (Lambda DNA/HindIII Marker; Thermo Scientific Fermentas); negative control (untreated plasmids); linear plasmid DNA (plasmids treated by EcoRI-HF, New England Biolabs Inc.); nicked open circular and linear plasmid DNA (plasmids treated with Fe^{2+} and H_2O_2); H_2O_2 negative control; test NPs negative control; series of reaction mixtures containing H_2O_2 and increasing concentrations of: CeO_2 NPs in DIW (A) and in ASW (B), ZnO NPs in DIW (C) and in ASW (D), MnO_2 NPs in DIW (E) and in ASW (F). On the right side of each picture, the white arrow points to undamaged DNA (i.e. supercoiled plasmid DNA), whereas the black arrow to ROS damaged DNA (i.e. nicked open circular and linear plasmid). In picture F, the simbol (*) marks the lack of damaged DNA in the MnO_2 NPs reaction mixtures in ASW. Abbreviation: *na*, not applicable.
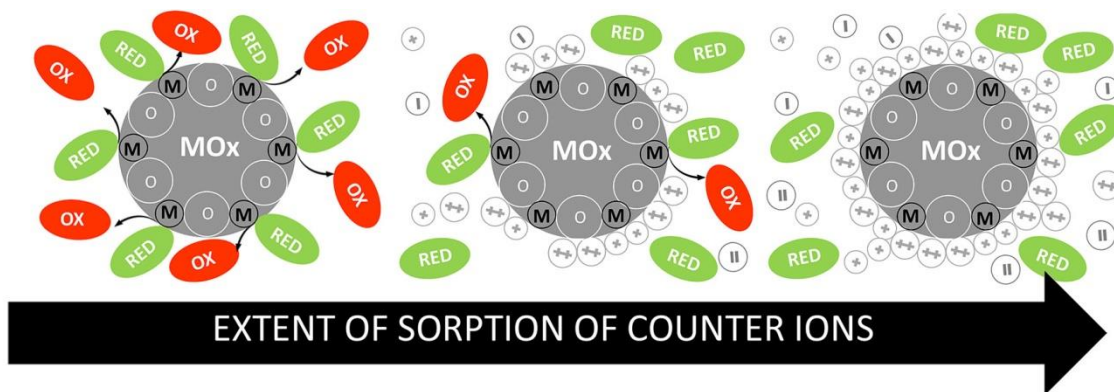
25

Figure 8 Schematic representation of the surface reactivity of MOx NPs having different ability to adsorb seawater cations (i.e. different pH_{IEP}).